ORIGINAL ARTICLE

# Heterophase junction engineering-induced Co spin-state modulation of CoSe₂ for large-current hydrogen evolution reaction

**Bao-Chai Xu, Ya-Ping Miao, Min-Qin Mao, Dong-Lian Li, Song Xie, Wei-Hong Jin, Shu Xiao, Jing Wen, Zaenab Abd-Allah, Zhi-Tian Liu, Xiang Peng\*, Paul K. Chu**

**Abstract** Efficient electrocatalysts are vital to large-current hydrogen production in commercial water splitting for green energy generation. Herein, a novel heterophase engineering strategy is described to produce polymorphic CoSe₂ electrocatalysts. The composition of the electrocatalysts consisting of both cubic CoSe₂ (c-CoSe₂) and orthorhombic CoSe₂ (o-CoSe₂) phases can be controlled precisely. Our results demonstrate that junction-induced spin-state modulation of Co atoms enhances the adsorption of intermediates and accelerates charge transfer resulting in superior large-current hydrogen evolution reaction (HER) properties. Specifically, the CoSe₂-based heterophase catalyst with the optimal c-CoSe₂ content requires an overpotential of merely 240 mV to achieve 1,000 mA·cm⁻² as well as a Tafel slope of 50.4 mV·dec⁻¹. Furthermore, the electrocatalyst can maintain a large current density of 1,500 mA·cm⁻² for over 320 h without decay. The results reveal the advantages and potential of heterophase junction engineering pertaining to design and fabrication of low-cost transition metal catalysts for large-current water splitting.

**Keywords** Heterophase junction; Spin-state; Hydrogen evolution reaction; Large current electrochemical hydrogen production; Water splitting

B.-C. Xu, M.-Q. Mao, D.-L. Li, S. Xie, J. Wen, Z.-T. Liu, X. Peng\*
Hubei Key Laboratory of Plasma Chemistry and Advanced Materials, School of Materials Science and Engineering, Wuhan Institute of Technology, Wuhan 430205, China
e-mail: xpeng@wit.edu.cn

Y.-P. Miao
School of Textile Science and Engineering, Xi'an Polytechnic University, Xi'an 710048, China

W.-H. Jin
Institute of Advanced Wear and Corrosion Resistant and Functional Materials, Jinan University, Guangzhou 510632, China

S. Xiao
Institute of Safety Science and Engineering, South China University of Technology, Guangzhou 510641, China

Z. Abd-Allah
Department of Engineering, Manchester Metropolitan University, Manchester M15 6BH, UK

P. K. Chu
Department of Physics, Department of Materials Science and Engineering, and Department of Biomedical Engineering, City University of Hong Kong, Hong Kong 999077, China

## 1 Introduction

Electrochemical water splitting is a promising hydrogen production technique offering a cleaner and more sustainable alternative to traditional pyrolysis of petrochemical products that generate carbon emissions. However, commercial adoption has been hindered by the limited availability and high cost of precious metal catalysts, particularly Pt and Pd, which are so far essential to the hydrogen evolution reaction (HER) [1–3]. Therefore, low-cost and efficient electrocatalysts are crucial to commercial water splitting for green energy generation. Moreover, industrial water splitting systems are typically operated at large current densities ($\geq$ 500 mA·cm⁻²) for extended periods and the electrocatalysts must be able to tolerate harsh conditions such as high pressure and temperature for a long period of time at large current densities [4, 5]. These

conditions are challenging and require durable and robust materials [6]. In this respect, low-cost alternative catalysts that can deliver large current densities are crucial to the development of commercial water splitting [7].

Earth-abundant, non-noble transition metal-based electrocatalysts such as transition metal chalcogenides [8–11], phosphides [12, 13], nitrides [14, 15], carbides [16, 17], and alloys [18, 19] have been proposed to substitute for precious metals for HER. In particular, cobalt selenide is known for its excellent electrocatalytic activity, high electrical conductivity, and efficient electron transfer in electrocatalysis [20, 21]. $CoSe_2$ generally exists in two phases, cubic (c-$CoSe_2$) and orthorhombic (o-$CoSe_2$), which undergo reversible transformation due to the similar atomic arrangements of cubic pyrite $CoSe_2$(100) and orthorhombic marcasite $CoSe_2$(101) [22]. Yu et al. have described the phosphorus-doping-induced phase transition from the cubic to orthorhombic phases in $CoSe_2$ and found an overpotential of 104 mV at 10 mA·cm$^{-2}$ in 1 mol·L$^{-1}$ KOH, onset potential of − 31 mV, and negligible activity decay after 20 h due to the favorable electronic structure and local coordination environment created by the phase transition [23]. They have subsequently proposed alkali-heated synthesis to prepare mixed-phase $CoSe_2$ using c-$CoSe_2$ as the precursor to obtain a nearly homogeneous distribution of cubic and orthorhombic phases, which requires an overpotential of 124 mV for 10 mA·cm$^{-2}$ and good durability for 400 h [22]. The mixture of o-$CoSe_2$ and c-$CoSe_2$ offers a significant advantage in that it enhances the covalent bonding between cobalt and selenium atoms. However, it is important to note that Co atoms have unpaired spin electrons which produce spin magnetic effects that can affect the electrocatalytic properties [24, 25]. The splitting energy and electron pairing energy of Co ions are relatively close, rendering them possible to obtain different spin-states by proper strategies [26, 27]. However, the impact of spin-state changes during the phase transition from o-$CoSe_2$ to c-$CoSe_2$ on the HER performance is not well understood, especially for large-current density HER in which efficient mass transfer and charge transport are critical. In fact, modulation of the spin-state of Co atoms in $CoSe_2$ from the perspective of HER optimization at large current densities has seldom been reported and is also quite challenging.

Herein, heterophase junction engineering is implemented to construct a composite electrocatalyst on carbon cloth (CC) consisting of o-$CoSe_2$ and c-$CoSe_2$ with a distinct heterophase interface between the two phases. Since the contents of o-$CoSe_2$ and c-$CoSe_2$ in the composite can be modulated precisely by this technique, the spin-state of Co atoms at the heterophase interface can be tuned to expose more active sites, improve hydrogen adsorption, accelerate charge transfer, and improve the catalytic characteristics. The optimized catalyst delivers excellent HER performance at a large current density as exemplified by a small overpotential of 240 mV for a large current density of 1,000 mA·cm$^{-2}$ in addition to exceptional stability in an acidic medium at an extremely large current density of 1,500 mA·cm$^{-2}$ for 320 h. The excellent HER properties are attributed to the regulated spin-state of Co atoms, abundant active hydrogen adsorption centers, and fast charge transfer. The novel heterophase junction engineering can be extended to construct stable and excellent electrodes composed of low-cost transition metal-based electrocatalysts for water splitting and other electrocatalysis.

## 2 Experimental

### 2.1 Materials preparation

1 mmol cobalt nitrate hexahydrate, 3 mmol ammonium fluoride, and 5 mmol urea were added to 30 ml deionized water (DW), stirred for 30 min, transferred to a Teflon lined autoclave containing a piece of clean CC (2 cm × 3 cm), and heated to 100 °C for 8 h. After cooling, the product was rinsed several times with DW, dried, and designated as $Co(OH)_2$/CC.

6 mmol selenium powder and the $Co(OH)_2$/CC precursor were placed in the upstream area and downstream area of the dual-temperature tube furnace, respectively. The furnace was heated to 340–600 °C for 1 h under an $H_2/N_2$ atmosphere with 8% $H_2$. The products were designated as pure cubic $CoSe_2$ (c-$CoSe_2$), pure orthorhombic $CoSe_2$ (o-$CoSe_2$), and composites (n-c-$CoSe_2$), where $n$ represents the content of c-$CoSe_2$ in the composite as a percentage.

### 2.2 Materials characterization

Scanning electron microscopy (SEM) was performed on the FEI/Philips XL30 Esem-FEG instrument and transmission electron microscopy (TEM) was carried out on the FEI/Philips Tecnai 12 BioTWIN. A high-resolution TEM (HRTEM) equipped with energy-dispersive spectroscopy (EDS) was used to study the detailed crystal structure and composition of the samples. X-ray diffraction (XRD) was conducted on the LabX XRD-6100 instrument with a Cu K$_\alpha$ source to determine the crystal structure and phase composition. The Raman scattering spectra were collected on the HR RamLab instrument to investigate the vibrational modes and X-ray photoelectron spectroscopy (XPS) was carried out on the Thermo Scientific K-Alpha instrument with monochromatic Al Kα X-ray to determine the chemical states. X-ray absorption spectra (XAS) including X-ray absorption near-edge structure (XANES) and extended X-ray absorption fine structure (EXAFS) of the

sample at Co K-edge were collected at the 1W1B station of Beijing Synchrotron Radiation Facility (BSRF), China.

## 2.3 Electrochemical measurement

The electrochemical measurements were taken on the CHI 660E electrochemical workstation (Shanghai CH Instrument, China) in a 0.5 mol·L$^{-1}$ H$_2$SO$_4$ aqueous solution. A three-electrode system in which a graphite rod served as the counter electrode, a saturated calomel electrode (SCE) was the reference electrode, and modified CC acted as the working electrode was employed. Linear sweep voltammetry (LSV) was conducted at a scanning rate of 5 mV·s$^{-1}$ and all the potentials were corrected with 80% $iR$ and referred to the reversible hydrogen electrode (RHE) based on Nernst equation $E_{(RHE)} = E_{(SCE)} + 0.242 + 0.059 \times$ pH, where the pH of the 0.5 mol·L$^{-1}$ H$_2$SO$_4$ electrolyte was determined to be 0.50 by the FE28 pH meter (Mettler Toledo). The Tafel slopes were derived by fitting the linear portion of the Tafel plots. Electrochemical impedance spectroscopy (EIS) was performed with an amplitude of 5 mV in the frequency range from 100,000 to 0.1 Hz at an initial potential of $-$ 0.4 V vs. SCE. The electrochemically active surface area (ECSA) was calculated from the cyclic voltammetry (CV) data in the voltage range of 0–0.1 V vs. SCE and the stability was evaluated by recording the HER current densities at constant potentials at different times.

## 2.4 Density-functional theory calculation

The calculation was performed with the Vienna Ab Initio Simulation Package (VASP) [28]. The spin-unrestricted PAW-PBE function was utilized to evaluate the exchange and correlation energies and the structures were relaxed using the conjugate gradient algorithm implemented in the VASP code. The convergence criteria for the forces and total energies on all the atoms were set to be less than 0.2 eV·nm$^{-1}$ and $1 \times 10^{-4}$ eV, respectively, and the kinetic energy cutoff was 500 eV. To model the heterophase junction of CoSe$_2$, a slab model consisting of six layers of Co and Se atoms was employed. The $3 \times 3 \times 1$ k-mesh was employed for Brillouin zone integration with a 1.5 nm thick vacuum layer included to avoid possible interactions.

## 3 Results and discussion

Figure 1a illustrates the phase conversion of CoSe$_2$ during selenation. Co(OH)$_2$ is prepared hydrothermally and o-CoSe$_2$ is produced by chemical vapor deposition (CVD) with Se powder as the source. When the temperature is increased, o-CoSe$_2$ morphs into c-CoSe$_2$ gradually. Owing

to the volume change during the transition from Co(OH)$_2$ to o-CoSe$_2$ and c-CoSe$_2$, a rough surface with more exposed active sites is created. The heterophase junction between o-CoSe$_2$ and c-CoSe$_2$ is formed during phase conversion, and more importantly, the amount of each phase can be modulated precisely. Hence, the electronic configuration of the atoms at the interface can be regulated to optimize hydrogen adsorption and charge transfer efficiency in HER. SEM images of the Co(OH)$_2$ precursor in Figs. S1a, 1b and c reveal nanowire arrays with a smooth surface around CC. After selenation at 340–400 °C, the array structure remains, although the nanowires become rough on the surface and there are surface humps as shown in Figs. S1b, S2a–d, 1d and e, which are in fact beneficial as a result of exposure of more active sites. Moreover, the nanowire arrays around the carbon fibers provide open channels for electrolyte diffusion and gaseous product evolution giving rise to fast kinetics. Nevertheless, the nanowire structure collapses when the temperature is over 450 °C (Fig. S2e–h) resulting in fewer surface sites exposure and poorer catalytic activity.

TEM image of the annealed product in Fig. 1f discloses nanowires with a diameter of $\sim$ 150 nm and a rough surface similar to that observed by SEM. HRTEM image in Fig. 1g exhibits clear fringe spacings of 0.248 and 0.202 nm ascribed to the o-CoSe$_2$ (120) and c-CoSe$_2$ (220) planes, respectively. More importantly, there is a clear heterophase junction at the interface between the o-CoSe$_2$ (120) and c-CoSe$_2$ (220) planes. The heterophase junction produces lattice mismatch and electronic structure modification at the interface to alter the adsorption behavior of reactants/intermediates/products and charge transfer during electrocatalysis. Figure 1h shows selected area electron diffraction (SAED) pattern which is consistent with the information imparted by HRTEM. The (011), (120), (210) and (220) planes of o-CoSe$_2$ and (220), (222) and (400) planes of c-CoSe$_2$ match JCPDS Nos. 53-0449 and 65-3327, respectively. The elemental maps in Fig. 1i reveal that Co and Se are distributed uniformly in the nanowires.

The Raman scattering spectra in Fig. 2a show peaks at 484 and 524 cm$^{-1}$ related to the E$_g$ and E$^1_{2g}$ modes of the tetrahedral and octahedral sites and that at 692 cm$^{-1}$ corresponds to the A$_{1g}$ mode of the octahedral sites of o-CoSe$_2$ in line with the literature [29, 30]. The peaks at 462, 508 and 664 cm$^{-1}$ associated with the cubic phase of CoSe$_2$ are located at smaller wavenumbers than those of o-CoSe$_2$ [29, 31]. When the reaction temperature goes up, the peaks shift gradually to smaller wavenumbers indicative of phase transition from orthorhombic to cubic.

The crystal structure and composition are determined by XRD, as shown in Figs. S3, 2b. The diffraction peaks at 30.8°, 34.5°, 40.0° and 47.7° of the sample prepared at 340 °C can be indexed to the (101), (111), (210) and (211)
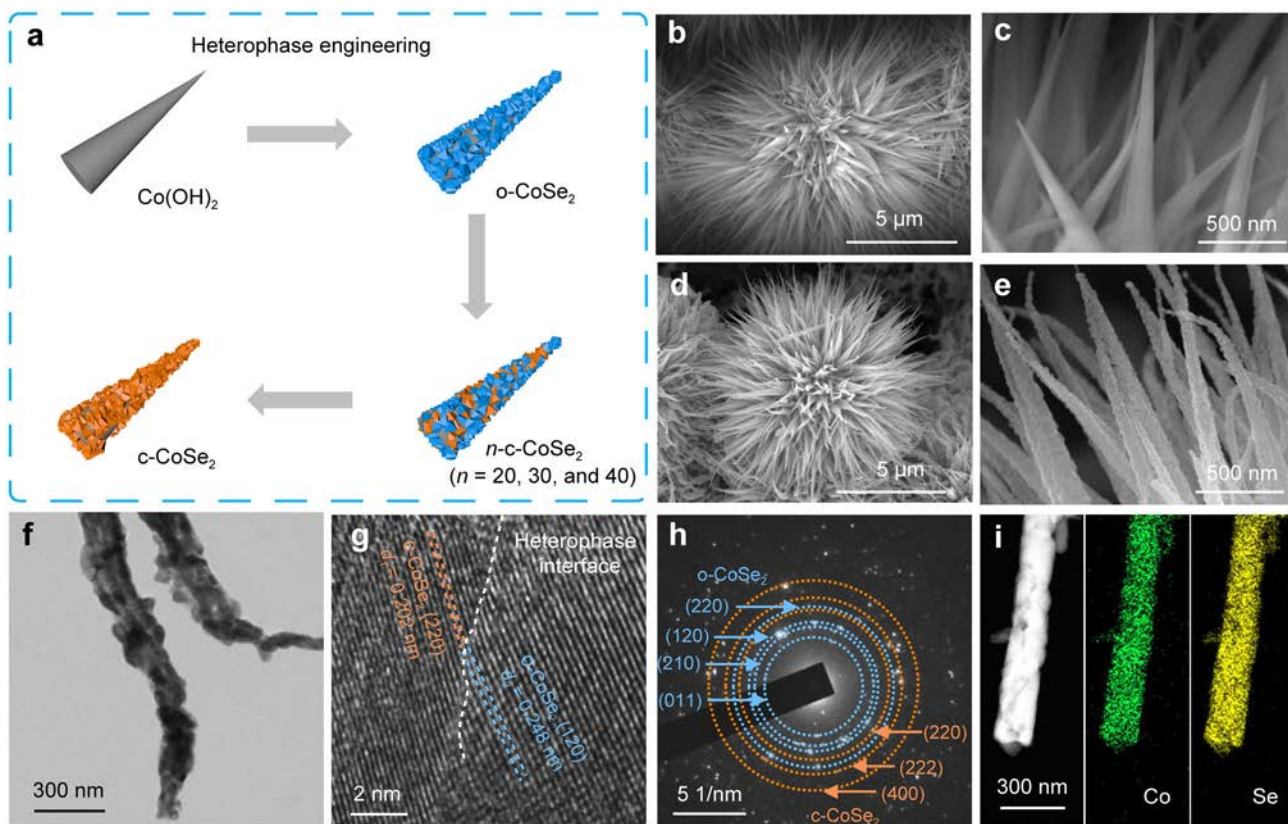
**Fig. 1** **a** Schematic illustration of heterophase junction engineering of CoSe$_2$; SEM images of **b**, **c** Co(OH)$_2$ precursor and **d**, **e** samples annealed at 400 °C; **f** TEM image, **g** HRTEM image, **h** SAED pattern and **i** elemental maps of 30-c-CoSe$_2$
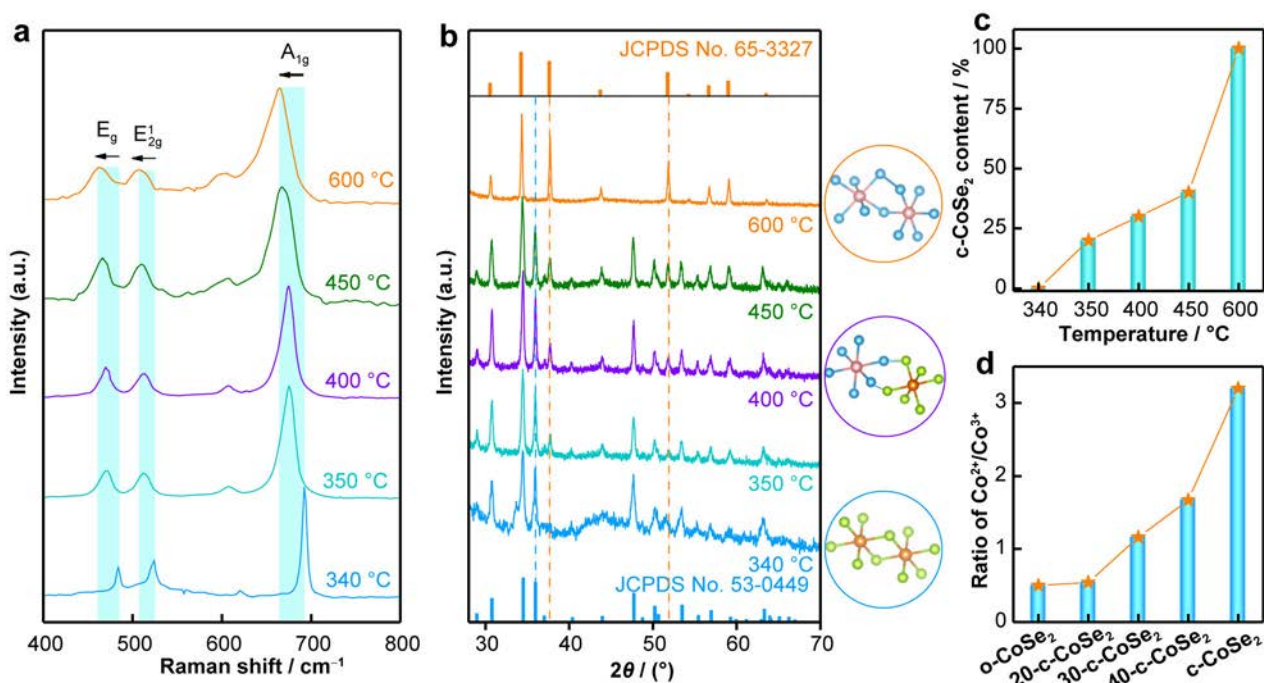


**Fig. 2** **a** Raman scattering spectra; **b** XRD patterns with corresponding bonding structures shown on right (dotted lines marking intensity changes); **c** c-CoSe$_2$ contents as a function of reaction temperature; **d** Co$^{2+}$/Co$^{3+}$ of catalysts with different c-CoSe$_2$ contents

planes of o-CoSe$_2$ (JCPDS No. 53-0449). As the temperature goes up, the diffraction peaks of o-CoSe$_2$ weaken, while the signal from the c-CoSe$_2$ phase appears. When the temperature is 600 °C, the pure c-CoSe$_2$ phase is indicated by peaks at 30.5°, 34.2°, 37.6° and 43.7° stemming from the (200), (210), (211) and (220) planes of c-CoSe$_2$ (JCPDS No. 65-3327), suggesting that the o-CoSe$_2$ phase is produced at a low temperature but converted into c-CoSe$_2$ with temperature increasing. Based on the intensity of the diffraction peaks, the amounts of the two phases are estimated and presented in Table S1 and Fig. 2c, which show that the c-CoSe$_2$ phase increases with temperature increasing. The pure phase of o-CoSe$_2$ and c-CoSe$_2$ can be obtained at 340 and 600 °C, respectively. When the temperature is 350, 400, and 450 °C, the products contain both o-CoSe$_2$ and c-CoSe$_2$ with the c-CoSe$_2$ concentration being 20%, 30% and 40%, respectively ($n$-c-CoSe$_2$, where $n$ = 20, 30 or 40). The change in the c-CoSe$_2$ phase gives rise to regulated electronic interactions and active sites at the interface which impacts the electrocatalytic properties.

Co and Se are observed from the survey XPS spectra in Fig. S4. The high-resolution spectra of Co 2p in Fig. S5 can be deconvoluted into Co$^{3+}$ peaks at 779.0 eV for Co 2p$_{3/2}$ and 794.0 eV for Co 2p$_{1/2}$ as well as Co$^{2+}$ at 780.7 eV for Co 2p$_{3/2}$ and 796.4 eV for Co 2p$_{1/2}$ [32, 33]. The peaks at 784.6 and 801.2 eV are satellite peaks. The peak area of Co$^{2+}$ increases while the area of Co$^{3+}$ decreases with temperature increasing (Fig. 2d and Table S2), indicating that the amount of surface Co$^{2+}$ goes up with the c-CoSe$_2$ phase increasing in the composite, which may result from the interaction between the CoSe$_2$ and elemental Se adsorbed at the surface [34, 35]. A larger Co$^{2+}$ concentration facilitates the adsorption of hydrogen to form Co–H bonds and accelerates electron transfer to enhance the HER activity [36].

Furthermore, synchrotron-based X-ray absorption fine structure spectroscopy (XAFS) was conducted to investigate the local structure of CoSe$_2$ using a Co foil as a contrast sample. Figure 3a shows XANES spectra of o-CoSe$_2$, 30-c-CoSe$_2$ and c-CoSe$_2$ at the Co K-edge, which show the pre-edge feature indicates that Co ions are in the octahedral environment [37]. The absorption edges of the samples shift slightly toward lower energy with the c-CoSe$_2$ concentration increasing corresponding to a lower valence state Co species, which agrees well with the increased Co$^{2+}$ revealed by XPS results. Figure 3b displays the corresponding Fourier transforms of the $k^3$-weighted extended X-ray absorption fine structure oscillations (FT-EXAFS) for the o-CoSe$_2$, 30-c-CoSe$_2$ and c-CoSe$_2$. The o-CoSe$_2$, 30-c-CoSe$_2$ and c-CoSe$_2$ samples exhibit strong peaks at ∼ 0.21 nm, which can be assigned to the typical Co-Se bond in different phases [38]. The

peak located at ∼ 0.22 nm for Co foil results from the Co–Co bond [39]. In addition, the wavelet transform (WT) contour plots of o-CoSe$_2$, 30-c-CoSe$_2$ and c-CoSe$_2$ are required to analyze the localized coordination environments (Fig. 3c−f). The WT maximum intensity for c-CoSe$_2$ is 109.6 nm$^{-1}$, while it is 108.4 nm$^{-1}$ for 30-c-CoSe$_2$ and 102.2 nm$^{-1}$ for o-CoSe$_2$, probably originating from the difference of Co-Se bonds in o-CoSe$_2$ and c-CoSe$_2$ [23, 40], associated with the unsaturated sites and defects at the surface [41]. Hence, XPS and XAFS results clearly demonstrate that the heterophase structure produces the optimized electronic structure and local coordination environment of CoSe$_2$ to modulate the hydrogen adsorption behavior and enhance the electrocatalytic properties.

Figure 4a shows the phase conversion from o-CoSe$_2$ to c-CoSe$_2$. In both phases, the Co atom is octahedrally bonded to the adjacent Se atom. However, the octahedra are corner-shared in the cubic pyrite type, while they are edge-shared in the orthorhombic marcasite type [42]. The heterophase interface is composed of o-CoSe$_2$(120) and c-CoSe$_2$(220) planes as revealed by HRTEM. The Co$^{2+}$ has two electronic configurations according to the number of unpaired 3d electrons, namely the low spin-state (t$_{2g}^6$ e$_g^1$) with one unpaired 3d electron and the high spin-state (t$_{2g}^5$ e$_g^2$) with three unpaired 3d electrons (Fig. S6a, b). The e$_g$ orbital is unevenly occupied, yielding a strong Jahn–Teller effect in both the low spin-state and high spin-state to produce a more distorted atomic arrangement in CoSe$_2$, giving rise to more active site exposure and optimal adsorption of hydrogen. The d-band centers of o-CoSe$_2$ and c-CoSe$_2$ are calculated to be –2.96 and –1.94 eV, respectively, while it is –1.79 eV for the heterophase junction (Fig. 4b). The notable up-shift of the d-band center demonstrates promoted hydrogen adsorption and hydrogen evolution [43]. The density of states (DOS) analysis in Fig. 4c indicates that the heterophase junction has a lot of new states that have been formed near the Fermi level ($E_F$) compared to o-CoSe$_2$ and c-CoSe$_2$ [44], in which the spin-up and spin-down channels are asymmetrical. As shown in Fig. S6c–e, the mid-gap states near the $E_F$ are mainly from the Co 3d orbitals on account of the strong Jahn–Teller effect [45]. The Co 3d orbitals induce strong hybridization in the energy range of − 1.8 to − 0.7 eV in the spin-up and spin-down channels. The states across the $E_F$ are contributed by Co-d$_{z^2}$ and Co-d$_{x^2−y^2}$, while the states in the energy range of − 1.8 to − 0.7 eV are contributed by Co-d$_{xy}$, Co-d$_{xz}$, and Co-d$_{yz}$, indicating the hybridization between Co atoms either directly or via the intervening Se orbitals. The total magnetic moment of the heterophase junction is 4.70 μB which is larger than those of o-CoSe$_2$ (0.55 μB) and c-CoSe$_2$ (1.72 μB), as shown in Fig. 4d, and mainly contributed by the Co atoms. Additionally, the
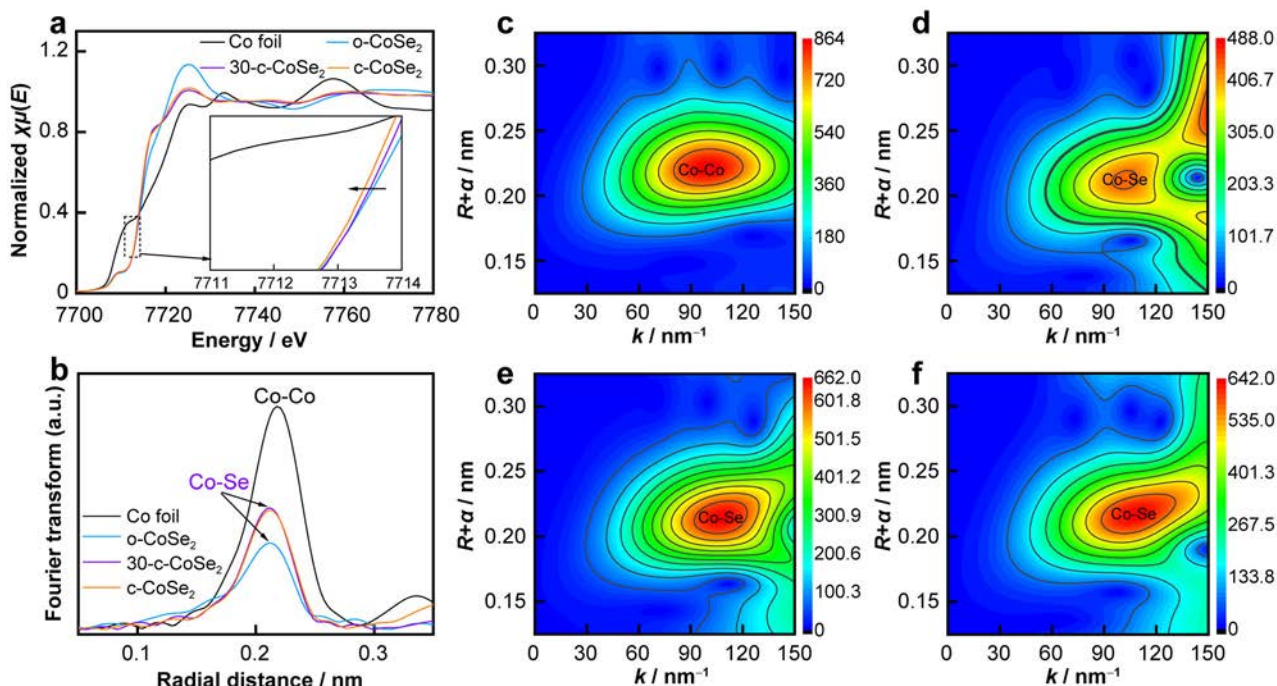
**Fig. 3** **a** XANES spectra recorded at Co K-edge; **b** corresponding FT-EXAFS spectra; wavelet transform spectra of **c** Co foil, **d** o-CoSe$_2$, **e** 30-c-CoSe$_2$ and **f** c-CoSe$_2$
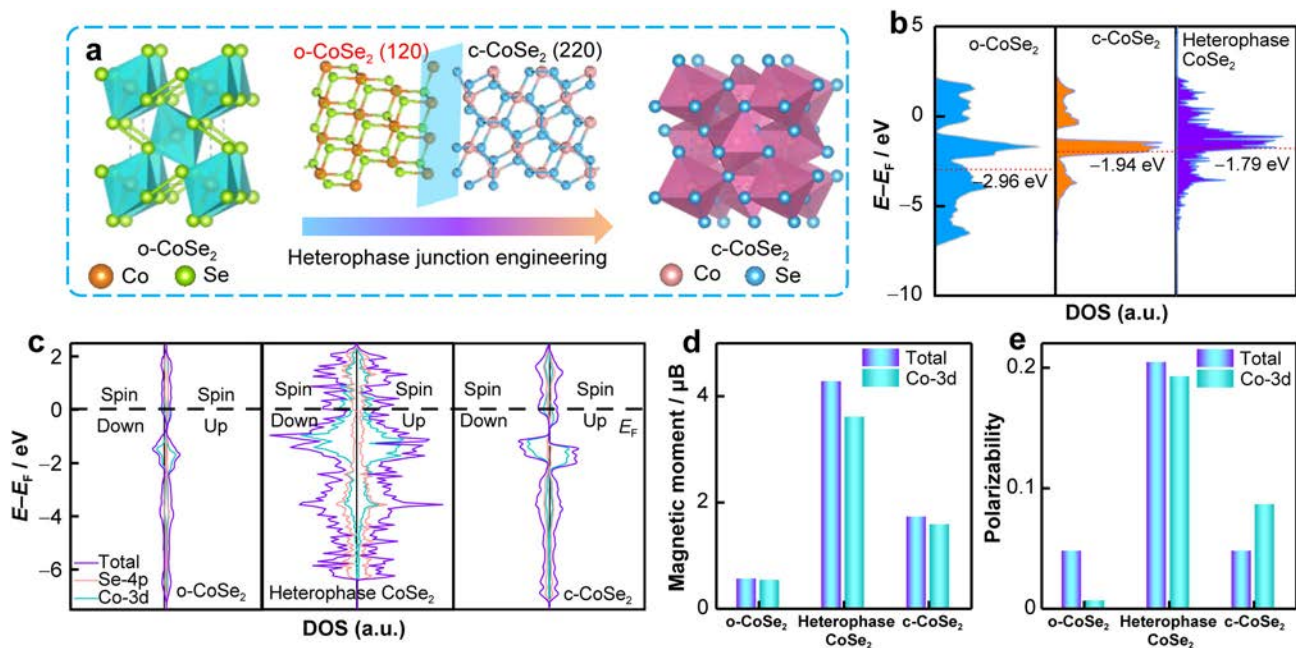


**Fig. 4** **a** Schematic illustration showing phase conversion from o-CoSe$_2$ to c-CoSe$_2$ via heterophase junction engineering; **b** d-band center diagrams; **c** DOS diagrams; **d** magnetic moment and **e** polarizability of o-CoSe$_2$, c-CoSe$_2$ and heterophase CoSe$_2$

specific spin polarizability shown in Fig. 4e (Supporting note 1) indicates that the pristine o-CoSe$_2$ and c-CoSe$_2$ show very weak spin polarization, whereas the formation of heterophase junction results in strong spin polarization, which may lead to fast charge transfer [46]. Therefore,

optimization the spin-state of the Co atoms at the heterophase interface may contribute to accelerated HER, especially at a large current.

The HER characteristics of the electrocatalysts are investigated using a three-electrode configuration in the

0.5 mol·L$^{-1}$ H$_2$SO$_4$ electrolyte. Figures S7, 5a show LSV curves, indicating that 30-c-CoSe$_2$ can afford a current density of 10 mA·cm$^{-2}$ at an overpotential of only 130 mV, which is smaller than those of transition metal chalcogenides such as MoS$_2$/graphene (183 mV) [47], α-MoB$_2$ (149 mV) [48], CoSe$_2$-450 (165 mV) [49], and CoSe/MoSe$_2$ (192 mV) [50]. The excellent HER activity of 30-c-CoSe$_2$ arises from the synergistic effects of the heterophase junction, moderated Co$^{2+}$ concentration at the surface, optimized spin-state, more active sites, and higher charge transfer efficiency. The electrocatalysts achieve a large current density of 1,000 mA·cm$^{-2}$. In particular, 30-c-CoSe$_2$ requires an overpotential of merely 240 mV to generate 1,000 mA·cm$^{-2}$, which is superior to o-CoSe$_2$ (560 mV), 20-c-CoSe$_2$ (474 mV), 40-c-CoSe$_2$ (306 mV), and c-CoSe$_2$ (511 mV), as shown in Table S3. The ECSA related to the number of surface-active sites is normally determined by the electrochemical double-layer capacitance ($C_{dl}$). The $C_{dl}$ values of the electrocatalysts calculated from the CV curves are presented in Fig. S8. Figure 5b and Table S3 show that 30-c-CoSe$_2$ has a $C_{dl}$ value of 35.8 mF·cm$^{-2}$ that is much larger than those of o-CoSe$_2$ (23.1 mF·cm$^{-2}$), 20-c-CoSe$_2$ (32.8 mF·cm$^{-2}$), 40-c-CoSe$_2$ (26.4 mF·cm$^{-2}$), and c-CoSe$_2$ (23.7 mF·cm$^{-2}$). Generally, a larger $C_{dl}$ translates into more active site exposure and better catalytic activity. LSV curves of the electrocatalysts based on the ECSA shown in Fig. S9 suggests the enhanced intrinsic activity of the 30-c-CoSe$_2$

compared to the pure o-CoSe$_2$ and c-CoSe$_2$, possibly originating from the heterophase junction-induced optimization of the active center.

The Tafel plots are produced to understand the HER kinetics, as shown in Fig. 5c. The Tafel slope (Table S3) of 30-c-CoSe$_2$ electrocatalyst is 50.4 mV·dec$^{-1}$ which is distinctly smaller than those of o-CoSe$_2$ (75.4 mV·dec$^{-1}$), 20-c-CoSe$_2$ (67.8 mV·dec$^{-1}$), 40-c-CoSe$_2$ (50.9 mV·dec$^{-1}$) and c-CoSe$_2$ (66.9 mV·dec$^{-1}$) and even smaller than those observed from cobalt-based compounds such as Mo$_{0.6}$-CoSe$_2$ NS@NF (69 mV·dec$^{-1}$) [51], Co(S$_{0.71}$Se$_{0.29}$)$_2$ NPs (85.7 mV·dec$^{-1}$) [52], Sn-CoSe$_2$ (86.0 mV·dec$^{-1}$) [53], and CC/MOF-CoSe$_2$@MoSe$_2$ (96.61 mV·dec$^{-1}$) [54]. Figure 5d summarizes the overpotentials for 1,000 mA·cm$^{-2}$, Tafel slopes and ECSA of the electrocatalysts, and 30-c-CoSe$_2$ has the smaller overpotential, Tafel slope, and larger ECSA. EIS results in Figs. S10, 5e confirm the smaller charge transfer resistance of 30-c-CoSe$_2$ and faster HER kinetics. The comparison of overpotential and Tafel slope of 30-c-CoSe$_2$ with recently reported electrocatalysts, including (1) α-MoB$_2$ [48], (2) Ni$_2$P/NF [55], (3) nano-KFO/NF [56], (4) F-Co$_2$P/Fe$_2$P/IF [57], (5) Ta/TaS$_2$ [58], (6) CuMo$_6$S$_8$/Cu [59], (7) Ni$_{2(1-x)}$Mo$_{2x}$P [60], (8) Ni-Co-P/NF [61], (9) LiCoBPO [62], (10) HC-MoS$_2$/Mo$_2$C [63], (11) MoS$_x$-Fe@UiO-66-(OH)$_2$ [64] and (12) Co-NC-AF [65], is shown in Fig. 5f and Table S4. Clearly, the excellent HER performance of the heterophase-engineered composite electrocatalyst (30-c-CoSe$_2$)
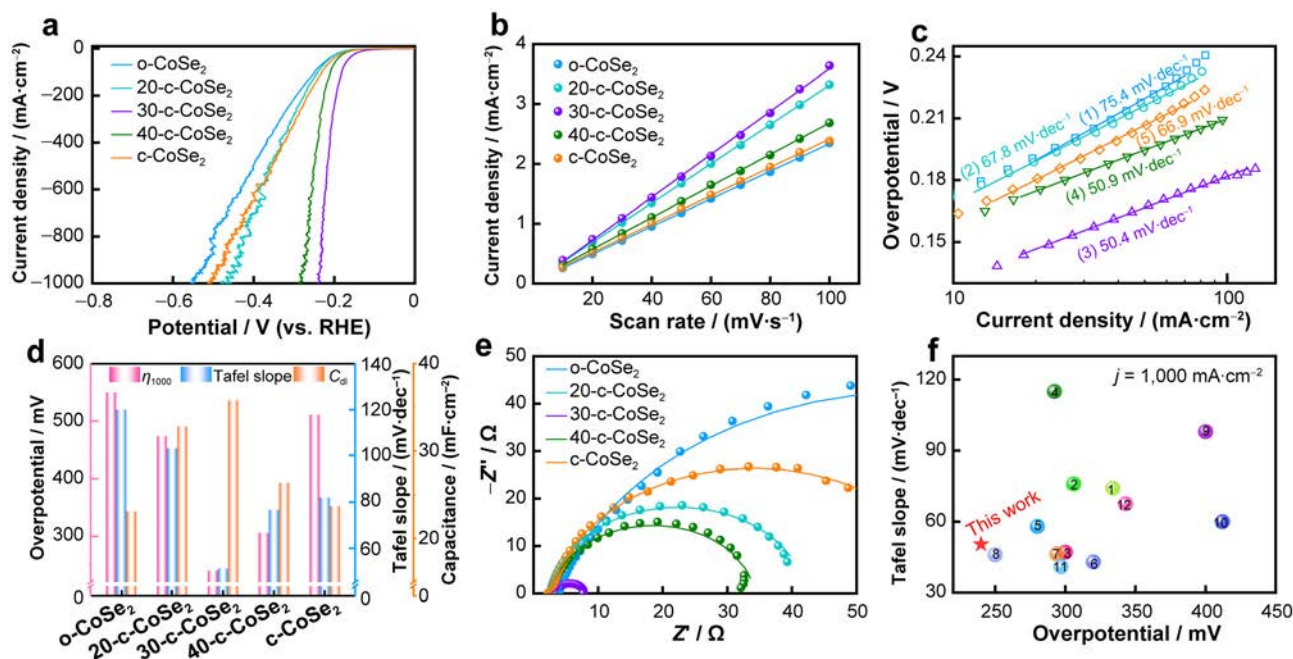


**Fig. 5** Electrochemical properties of different samples: **a** polarization curves; **b** ECSA; **c** Tafel plots; **d** comparison of overpotentials, Tafel slopes and ECSA; **e** EIS of (1) o-CoSe$_2$, (2) 20-c-CoSe$_2$, (3) 30-c-CoSe$_2$, (4) 40-c-CoSe$_2$ and (5) c-CoSe$_2$; **f** comparison of overpotential and Tafel slope of 30-c-CoSe$_2$ with those of typical transition metal-based electrocatalysts reported recently

is a result of the open and ordered structure of the nanowire arrays on the carbon fibers facilitating mass transport and gas release. Besides, the moderate $Co^{2+}$ concentration derived by the c-$CoSe_2$ phase improves the electron transfer efficiency and the heterophase interface between o-$CoSe_2$ and c-$CoSe_2$ increases the active centers and optimizes the electronic configuration for accelerated HER.

The robust stability is another key to commercial application and 30-c-$CoSe_2$ is evaluated by the chronoamperometric method at large current densities of 500, 1,000 and 1,500 mA·cm$^{-2}$, as shown in Figs. 6a, S11. The results disclose excellent stability even at an ultra-large current density of 1,500 mA·cm$^{-2}$ for 320 h as illustrated by the $i$-$t$ curve in Fig. 6a, which is superior to the previous $CoSe_2$ electrocatalysts as listed in Table S5. Meanwhile, the LSV curve shifts merely 25 mV at 1,000 mA·cm$^{-2}$, nearly the same as that acquired before the long-term test as revealed by Fig. 6b. The morphology and surface chemistry of the electrocatalyst after the test are examined and the nanowires with a rough surface are still surrounded by carbon fibers after operation for 320 h as shown in Fig. S12a, b. HRTEM image of 30-c-$CoSe_2$ electrocatalyst after the long-term test

in Fig. S13 indicates the lattices with spacings of 0.252 and 0.201 nm originated from o-$CoSe_2$ (120) and c-$CoSe_2$ (220) planes, respectively, which match well with the heterophase interface in the fresh sample. The survey XPS spectrum after the long-term test discloses the presence of Se, Co, C and O (Fig. S14a). The high-resolution Co 2p spectra in Fig. S14b show $Co^{3+}$ peaks at 778.9 eV for Co $2p_{3/2}$ and 793.7 eV for Co $2p_{1/2}$ as well as $Co^{2+}$ at 780.6 eV for Co $2p_{3/2}$ and 796.4 eV for Co $2p_{1/2}$, which are in line with those observed from the pristine sample. Additionally, the ratio of $Co^{2+}$/$Co^{3+}$ is calculated to be 1.13 which is also very close to the initial value. All these results suggest the excellent physical and chemical stability of 30-c-$CoSe_2$ electrocatalyst.

The Faraday efficiency of 30-c-$CoSe_2$ for HER is assessed as shown in Fig. 6c. The apparatus consists of a sealed H-type electrolytic cell with a proton exchange membrane that separates the anode and cathode. The volume of gas produced on the cathode is determined by the water displacement method. As shown in Fig. 6d, 53.0 ml hydrogen is produced during the continuous test for 70 min at a current of 100 mA, indicating a fast hydrogen production rate of 1.9 mmol·h$^{-1}$ in the acidic electrolyte.
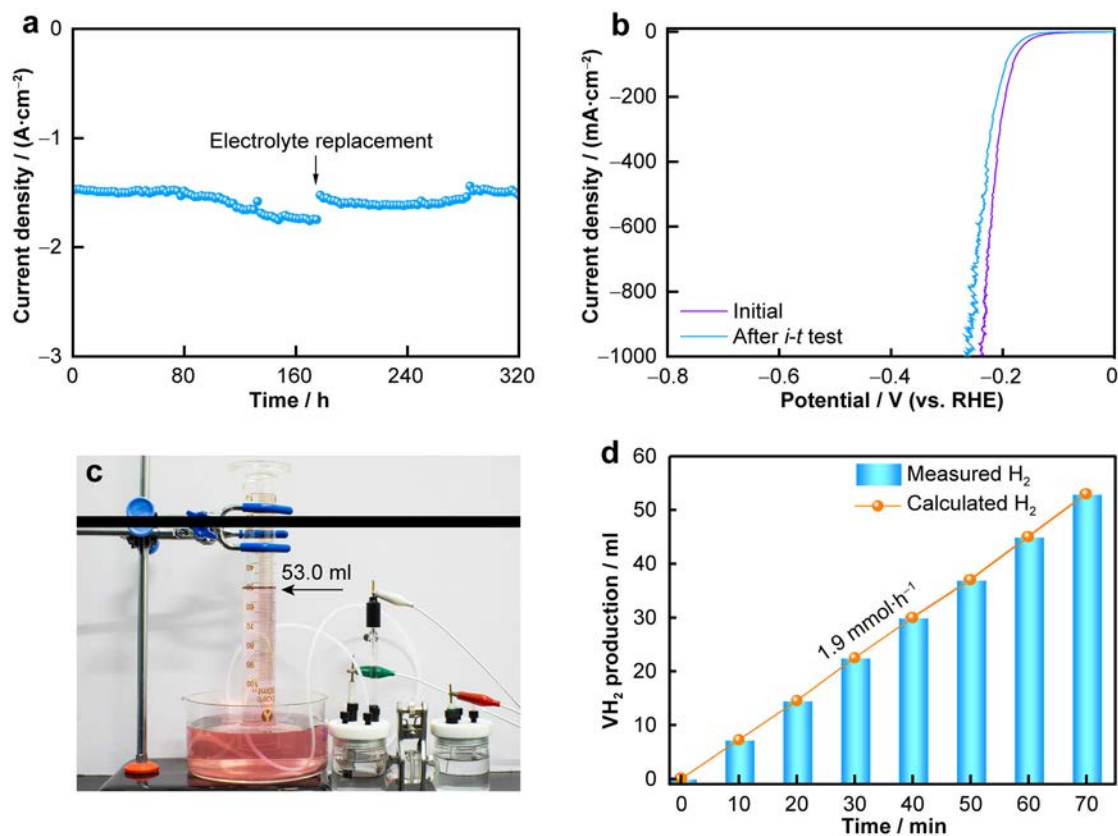


Fig. 6 a Stability evaluation of 30-c-$CoSe_2$ electrocatalyst; b polarization curves acquired before and after long-term test on 30-c-$CoSe_2$; c photograph of HER system consisting of 30-c-$CoSe_2$ electrocatalyst and $H_2$ gas generation determined by water displacement method; d experimental and theoretical amounts of $H_2$ produced by 30-c-$CoSe_2$ at a current of 100 mA in 0.5 mol·L$^{-1}$ $H_2SO_4$

Furthermore, the Faraday efficiency is determined to be 99.6% (Supporting note 2), which is very close to the theoretical value.

## 4 Conclusion

The heterophase junction of o-CoSe$_2$/c-CoSe$_2$ is designed and fabricated by phase engineering. The spin-state of Co atoms at the heterophase interface is modulated to produce an up-shift of the d-band center, a closer position to the $E_F$ of the density of states, enhanced polarization of the Co 3d orbitals, optimized adsorption of intermediates, as well as accelerated charge transfer in electrocatalysis. As a result, the heterophase junction electrocatalyst delivers excellent HER performance as manifested by a small overpotential of 240 mV to achieve a current density of 1,000 mA·cm$^{-2}$ and exceptional stability at an ultra-large current density of 1,500 mA·cm$^{-2}$ for 320 h in an acidic media. The results reveal a novel strategy to improve the HER activity at large currents by tuning the spin-state of transition metal-based electrocatalysts. This precise phase engineering concept can be extended to form other types of heterophase junctions in electrocatalysts. This precise phase engineering strategy can be extended to produce other heterophase junctions of transition metal-based electrocatalysts for water splitting as well as other electrocatalysis.

**Declarations**

**Conflict of interests** The authors declare that they have no conflict of interest.

## References

[1] Yu DH, Zuo C, Gao Y, Zhou SP, Lu J, Liu F. Research progress on electrolysis of hydrogen-deposited noble metal electrocatalysts. Chin J Rare Met. 2023;47(11):1573. https://doi.org/10.13373/j.cnki.cjrm.XY19120030.

[2] Zhou F, Zhou Y, Liu GG, Wang CT, Wang J. Recent advances in nanostructured electrocatalysts for hydrogen evolution reaction. Rare Met. 2021;40(12):3375. https://doi.org/10.1007/s12598-021-01735-y.

[3] Wu T, Sun MZ, Huang BL. Non-noble metal-based bifunctional electrocatalysts for hydrogen production. Rare Met. 2022;41(7):2169. https://doi.org/10.1007/s12598-021-01914-x.

[4] King LA, Hubert MA, Capuano C, Manco J, Danilovic N, Valle E, Hellstern TR, Ayers K, Jaramillo TF. A non-precious metal hydrogen catalyst in a commercial polymer electrolyte membrane electrolyser. Nat Nanotechnol. 2019;14(11):1071. https://doi.org/10.1038/s41565-019-0550-7.

[5] Jin M, Zhang X, Niu S, Wang Q, Huang R, Ling R, Huang J, Shi R, Amini A, Cheng C. Strategies for designing high-performance hydrogen evolution reaction electrocatalysts at large current densities above 1000 mA cm$^{-2}$. ACS Nano. 2022;16(8):11577. https://doi.org/10.1021/acsnano.2c02820.

[6] Zhang C, Kremer MP, Seral-Ascaso A, Park S-H, McEvoy N, Anasori B, Gogotsi Y, Nicolosi V. Stamping of flexible, coplanar micro-supercapacitors using MXene inks. Adv Funct Mater. 2018;28(9):1705506. https://doi.org/10.1002/adfm.201705506.

[7] Anasori B, Lukatskaya MR, Gogotsi Y. 2D metal carbides and nitrides (MXenes) for energy storage. Nat Rev Mater. 2017;2(2):16098. https://doi.org/10.1038/natrevmats.2016.98.

[8] Peng X, Xie S, Wang X, Pi CR, Liu ZT, Gao B, Hu LS, Xiao W, Chu PK. Energy-saving hydrogen production by the methanol oxidation reaction coupled with the hydrogen evolution reaction co-catalyzed by a phase separation induced heterostructure. J Mater Chem A. 2022;10(39):20761. https://doi.org/10.1039/d2ta02955c.

[9] Sajjad S, Wang C, Deng CW, Ji F, Ali T, Shezad B, Ji HQ, Yan CL. Unravelling critical role of metal cation engineering in boosting hydrogen evolution reaction activity of molybdenum diselenide. Rare Met. 2022;41(6):1851. https://doi.org/10.1007/s12598-021-01948-1.

[10] Peng X, Xie S, Xiong S, Li R, Wang P, Zhang X, Liu Z, Hu L, Gao B, Kelly P, Chu PK. Ultralow-voltage hydrogen production and simultaneous Rhodamine B beneficiation in neutral wastewater. J Energy Chem. 2023;81:574. https://doi.org/10.1016/j.jechem.2023.03.022.

[11] Sun R, Su ZH, Zhao ZF, Yang MQ, Li TS, Zhao JX, Shang YC. Ni$_3$S$_2$ nanocrystals in-situ grown on Ni foam as highly efficient electrocatalysts for alkaline hydrogen evolution. Rare Met. 2023;42(10):3420. https://doi.org/10.1007/s12598-023-02337-6.

[12] Duan J, Chen S, Ortíz-Ledón CA, Jaroniec M, Qiao SZ. Phosphorus vacancies that boost electrocatalytic hydrogen evolution by two orders of magnitude. Angew Chem Int Ed. 2020;59(21):8181. https://doi.org/10.1002/anie.201914967.

[13] Guang HL, Zhu SL, Liang YQ, Wu SL, Li ZY, Luo SY, Cui ZD, Inoue A. Highly efficient nanoporous CoBP electrocatalyst for hydrogen evolution reaction. Rare Met. 2021;40(5):1031. https://doi.org/10.1007/s12598-020-01697-7.

[14] Sanati S, Morsali A, García H. First-row transition metal-based materials derived from bimetallic metal–organic frameworks as highly efficient electrocatalysts for electrochemical water splitting. Energy Environ Sci. 2022;15(8):3119. https://doi.org/10.1039/D1EE03614A.

[15] Huang C, Zhang XL, Tang J, Li D, Ruan QD, Liu LL, Xiong FY, Wang B, Xu Y, Cui SH, Luo Y, Li QW, Chu PK. Spatially strain-induced and selective preparation of Mo$_x$N ($x$=1, 2) as a highly efficient nanoarchitectonic catalyst for hydrogen evolution reaction in a wide pH range. Rare Met. 2023;42(5):1446. https://doi.org/10.1007/s12598-022-02227-3.

[16] Cui Y, Tan X, Xiao K, Zhao S, Bedford NM, Liu Y, Wang Z, Wu KH, Pan J, Saputera WH, Cheong S, Tilley RD, Smith SC, Yun J, Dai L, Amal R, Wang DW. Tungsten oxide/carbide surface heterojunction catalyst with high hydrogen evolution activity. ACS Energy Lett. 2020;5(11):3560. https://doi.org/10.1021/acsenergylett.0c01858.

[17] Fu W, Wang Y, Hu J, Zhang H, Luo P, Sun F, Ma X, Huang Z, Li J, Guo Z, Wang Y. Surface-electron coupling for efficient hydrogen evolution. Angew Chem Int Ed. 2019;58(49):17709. https://doi.org/10.1002/anie.201908938.

[18] Luo M, Yang J, Li X, Eguchi M, Yamauchi Y, Wang ZL. Insights into alloy/oxide or hydroxide interfaces in Ni–Mo-based electrocatalysts for hydrogen evolution under alkaline conditions. Chem Sci. 2023;14(13):3400. https://doi.org/10.1039/D2SC06298D.

[19] Zhang ZY, Tian H, Bian L, Liu SZ, Liu Y, Wang ZL. Cu-Zn-based alloy/oxide interfaces for enhanced electroreduction of $CO_2$ to $C_{2+}$ products. J Energy Chem. 2023;83:90. https://doi.org/10.1016/j.jechem.2023.04.034.

[20] Xu H, Ci S, Ding Y, Wang G, Wen Z. Recent advances in precious metal-free bifunctional catalysts for electrochemical conversion systems. J Mater Chem A. 2019;7(14):8006. https://doi.org/10.1039/C9TA00833K.

[21] Wang G, Chen J, Li K, Huang J, Huang Y, Liu Y, Hu X, Zhao B, Yi L, Jones TW, Wen Z. Cost-effective and durable electrocatalysts for Co-electrolysis of $CO_2$ conversion and glycerol upgrading. Nano Energy. 2022;92:106751. https://doi.org/10.1016/j.nanoen.2021.106751.

[22] Zhang XL, Hu SJ, Zheng YR, Wu R, Gao FY, Yang PP, Niu ZZ, Gu C, Yu X, Zheng XS, Ma C, Zheng X, Zhu JF, Gao MR, Yu SH. Polymorphic cobalt diselenide as extremely stable electrocatalyst in acidic media via a phase-mixing strategy. Nat Commun. 2019;10(1):5338. https://doi.org/10.1038/s41467-019-12992-y.

[23] Zheng YR, Wu P, Gao M-R, Zhang XL, Gao FY, Ju HX, Wu R, Gao Q, You R, Huang WX, Liu SJ, Hu SW, Zhu J, Li Z, Yu SH. Doping-induced structural phase transition in cobalt diselenide enables enhanced hydrogen evolution catalysis. Nat Commun. 2018;9(1):2533. https://doi.org/10.1038/s41467-018-04954-7.

[24] Lin L, Xin R, Yuan M, Wang T, Li J, Xu Y, Xu X, Li M, Du Y, Wang J, Wang S, Jiang F, Wu W, Lu C, Huang B, Sun Z, Liu J, He J, Sun G. Revealing spin magnetic effect of iron-group layered double hydroxides with enhanced oxygen catalysis. ACS Catal. 2023;13(2):1431. https://doi.org/10.1021/acscatal.2c04983.

[25] Liu Y, Hua X, Xiao C, Zhou T, Huang P, Guo Z, Pan B, Xie Y. Heterogeneous spin states in ultrathin nanosheets induce subtle lattice distortion to trigger efficient hydrogen evolution. J Am Chem Soc. 2016;138(15):5087. https://doi.org/10.1021/jacs.6b00858.

[26] Shen S, Wang Z, Lin Z, Song K, Zhang Q, Meng F, Gu L, Zhong W. Crystalline-amorphous interfaces coupling of $CoSe_2$/CoP with optimized d-band center and boosted electrocatalytic hydrogen evolution. Adv Mater. 2022;34(13):2110631. https://doi.org/10.1002/adma.202110631.

[27] Jin YZ, Li Z, Wang JQ, Li R, Li ZQ, Liu H, Mao J, Dong CK, Yang J, Qiao SZ, Du XW. Tuning spin state of rock-salt-based oxides by manipulation of crystallinity for efficient oxygen electrocatalysis. Adv Energy Mater. 2018;8(22):1703469. https://doi.org/10.1002/aenm.201703469.

[28] Kresse G, Hafner J. Ab initio molecular dynamics for liquid metals. Phys Rev B. 1993;47(1):558. https://doi.org/10.1103/PhysRevB.47.558.

[29] Li H, Qian X, Zhu C, Jiang X, Shao L, Hou L. Template synthesis of $CoSe_2$/$Co_3Se_4$ nanotubes: tuning of their crystal structures for photovoltaics and hydrogen evolution in alkaline medium. J Mater Chem A. 2017;5(9):4513. https://doi.org/10.1039/C6TA10718D.

[30] Windisch C Jr, Exarhos GJ, Ferris KF, Engelhard MH, Stewart DC. Infrared transparent spinel films with p-type conductivity. Thin Solid Films. 2001;398:45. https://doi.org/10.1016/S0040-6090(01)01302-5.

[31] Campos C, De Lima J, Grandi T, Machado K, Pizani P. Structural studies of cobalt selenides prepared by mechanical alloying. Physica B. 2002;324(1–4):409. https://doi.org/10.1016/S0921-4526(02)01461-8.

[32] Ma MY, Yu HZ, Deng LM, Wang LQ, Liu SY, Pan H, Ren JW, MY Maximov, Feng H, Peng SJ. Interfacial engineering of heterostructured carbon-supported molybdenum cobalt sulfides for efficient overall water splitting. Tungsten. 2023;5(4):589. https://doi.org/10.1007/s42864-023-00212-6.

[33] Hu J, Gao F, Zhao Z, Sang S, Li P, Zhang W, Zhou X, Chen Y. Synthesis and characterization of cobalt-doped ZnO microstructures for methane gas sensing. Appl Surf Sci. 2016;363:181. https://doi.org/10.1016/j.apsusc.2015.12.024.

[34] Peng X, Yan YJ, Xiong SJ, Miao YP, Wen J, Liu ZT, Gao B, Hu LS, Chu PK. Se-NiSe$_2$ hybrid nanosheet arrays with self-regulated elemental Se for efficient alkaline water splitting. J Mater Sci Technol. 2022;118:136. https://doi.org/10.1016/j.jmst.2021.12.022.

[35] Wang F, Li Y, Shifa TA, Liu K, Wang F, Wang Z, Xu P, Wang Q, He J. Selenium-enriched nickel selenide nanosheets as a robust electrocatalyst for hydrogen generation. Angew Chem Int Ed. 2016;55(24):6919. https://doi.org/10.1002/anie.201602802.

[36] Sun J, Li J, Li Z, Li C, Ren G, Zhang Z, Meng X. Modulating the electronic structure on cobalt sites by compatible heterojunction fabrication for greatly improved overall water/seawater electrolysis. ACS Sustain Chem Eng. 2022;10(30):9980. https://doi.org/10.1021/acssuschemeng.2c02571.

[37] de Groot F, Vankó G, Glatzel P. The 1s X-ray absorption pre-edge structures in transition metal oxides. J Phys: Condens Matter. 2009;21(10):104207. https://doi.org/10.1088/0953-8984/21/10/104207.

[38] Chen P, Xu K, Tao S, Zhou T, Tong Y, Ding H, Zhang L, Chu W, Wu C, Xie Y. Phase-transformation engineering in cobalt diselenide realizing enhanced catalytic activity for hydrogen evolution in an alkaline medium. Adv Mater. 2016;28(34):7527. https://doi.org/10.1002/adma.201601663.

[39] Mao J, He CT, Pei J, Chen W, He D, He Y, Zhuang Z, Chen C, Peng Q, Wang D, Li Y. Accelerating water dissociation kinetics by isolating cobalt atoms into ruthenium lattice. Nat Commun. 2018;9(1):4958. https://doi.org/10.1038/s41467-018-07288-6.

[40] Fei H, Dong J, Arellano-Jiménez MJ, Ye G, Dong Kim N, Samuel ELG, Peng Z, Zhu Z, Qin F, Bao J, Yacaman MJ, Ajayan PM, Chen D, Tour JM. Atomic cobalt on nitrogen-doped graphene for hydrogen generation. Nat Commun. 2015;6(1):8668. https://doi.org/10.1038/ncomms9668.

[41] Pi C, Li X, Zhang X, Song H, Zheng Y, Gao B, Kızılaslan A, Chu PK, Huo K. In-plane mott-schottky effects enabling efficient hydrogen evolution from $Mo_5N_6$-$MoS_2$ heterojunction nanosheets in universal-pH electrolytes. Small. 2022;18(22):2201137. https://doi.org/10.1002/smll.202201137

[42] Kong D, Wang H, Lu Z, Cui Y. $CoSe_2$ nanoparticles grown on carbon fiber paper: an efficient and stable electrocatalyst for hydrogen evolution reaction. J Am Chem Soc. 2014;136(13):4897. https://doi.org/10.1021/ja501497n.

[43] Chen Z, Song Y, Cai J, Zheng X, Han D, Wu Y, Zang Y, Niu S, Liu Y, Zhu J, Liu X, Wang G. Tailoring the d-band centers enables $Co_4N$ nanosheets to be highly active for hydrogen evolution catalysis. Angew Chem Int Ed. 2018;57(18):5076. https://doi.org/10.1002/anie.201801834.

[44] Sun M, Dougherty AW, Huang B, Li Y, Yan CH. Accelerating atomic catalyst discovery by theoretical calculations-machine learning strategy. Adv Energy Mater. 2020;10(12):1903949. https://doi.org/10.1002/aenm.201903949.

[45] Sampson MD, Park JS, Schaller RD, Chan MKY, Martinson ABF. Transition metal-substituted lead halide perovskite absorbers. J Mater Chem A. 2017;5(7):3578. https://doi.org/10.1039/C6TA09745F.

[46] Yin H, Chen Z, Xiong S, Chen J, Wang C, Wang R, Kuwahara Y, Luo J, Yamashita H, Peng Y, Li J. Alloying effect-induced electron polarization drives nitrate electroreduction to ammonia.

Chem Catal. 2021;1(5):1088. https://doi.org/10.1016/j.checat.2021.08.014.

[47] Sarwar S, Nautiyal A, Cook J, Yuan Y, Li J, Uprety S, Shahbazian-Yassar R, Wang R, Park M, Bozack MJ, Zhang X. Facile microwave approach towards high performance MoS$_2$/graphene nanocomposite for hydrogen evolution reaction. Sci China Mater. 2020;63(1):62. https://doi.org/10.1007/s40843-019-9555-0.

[48] Chen Y, Yu G, Chen W, Liu Y, Li G-D, Zhu P, Tao Q, Li Q, Liu J, Shen X, Li H, Huang X, Wang D, Asefa T, Zou X. Highly active, nonprecious electrocatalyst comprising borophene subunits for the hydrogen evolution reaction. J Am Chem Soc. 2017;139(36):12370. https://doi.org/10.1021/jacs.7b06337.

[49] Wang K, Xi D, Zhou C, Shi Z, Xia H, Liu G, Qiao G. CoSe$_2$ necklace-like nanowires supported by carbon fiber paper: a 3D integrated electrode for the hydrogen evolution reaction. J Mater Chem A. 2015;3(18):9415. https://doi.org/10.1039/C5TA01143D.

[50] Song W, Wang K, Jin G, Wang Z, Li C, Yang X, Chen C. Two-step hydrothermal synthesis of CoSe/MoSe$_2$ as hydrogen evolution electrocatalysts in acid and alkaline electrolytes. ChemElectroChem. 2019;6(18):4842. https://doi.org/10.1002/celc.201901382.

[51] Huang J, Wang S, Nie J, Huang C, Zhang X, Wang B, Tang J, Du C, Liu Z, Chen J. Active site and intermediate modulation of 3D CoSe$_2$ nanosheet array on Ni foam by Mo doping for high-efficiency overall water splitting in alkaline media. Chem Eng J. 2021;417:128055. https://doi.org/10.1016/j.cej.2020.128055.

[52] Fang L, Li W, Guan Y, Feng Y, Zhang H, Wang S, Wang Y. Tuning unique peapod-like Co(S$_x$Se$_{1-x}$)$_2$ nanoparticles for efficient overall water splitting. Adv Funct Mater. 2017;27(24):1701008. https://doi.org/10.1002/adfm.201701008.

[53] Liu C, Hu Y, Liu F, Liu H, Xu X, Xue Y, Zhang J, Li Y, Tang C. Electronic structure modulation of CoSe$_2$ nanowire arrays by tin doping toward efficient hydrogen evolution. Int J Hydrogen Energ. 2021;46(33):17133. https://doi.org/10.1016/j.ijhydene.2021.02.136.

[54] Patil SJ, Chodankar NR, Hwang SK, Shinde PA, Seeta Rama Raju G, Shanmugam Ranjith K, Huh YS, Han YK. Co-metal-organic framework derived CoSe$_2$@MoSe$_2$ core-shell structure on carbon cloth as an efficient bifunctional catalyst for overall water splitting. Chem Eng J. 2022;429:132379. https://doi.org/10.1016/j.cej.2021.132379.

[55] Yu X, Yu ZY, Zhang XL, Zheng YR, Duan Y, Gao Q, Wu R, Sun B, Gao MR, Wang G, Yu SH. "Superaerophobic" nickel phosphide nanoarray catalyst for efficient hydrogen evolution at ultrahigh current densities. J Am Chem Soc. 2019;141(18):7537. https://doi.org/10.1021/jacs.9b02527.

[56] Jian J, Chen W, Zeng D, Chang L, Zhang R, Jiang M, Yu G, Huang X, Yuan H, Feng S. Metal-ionic-conductor potassium ferrite nanocrystals with intrinsic superhydrophilic surfaces for electrocatalytic water splitting at ultrahigh current densities. J Mater Chem A. 2021;9(12):7586. https://doi.org/10.1039/D1TA00693B.

[57] Zhang XY, Zhu YR, Chen Y, Dou SY, Chen XY, Dong B, Guo BY, Liu DP, Liu CG, Chai YM. Hydrogen evolution under large-current-density based on fluorine-doped cobalt-iron phosphides. Chem Eng J. 2020;399:125831. https://doi.org/10.1016/j.cej.2020.125831.

[58] Yu Q, Zhang Z, Qiu S, Luo Y, Liu Z, Yang F, Liu H, Ge S, Zou X, Ding B, Ren W, Cheng H-M, Sun C, Liu B. A Ta-TaS$_2$ monolith catalyst with robust and metallic interface for superior hydrogen evolution. Nat Commun. 2021;12(1):6051. https://doi.org/10.1038/s41467-021-26315-7.

[59] Yu M, Wang Z, Liu J, Sun F, Yang P, Qiu J. A hierarchically porous and hydrophilic 3D nickel-iron/MXene electrode for accelerating oxygen and hydrogen evolution at high current densities. Nano Energy. 2019;63:103880. https://doi.org/10.1016/j.nanoen.2019.103880.

[60] Yu L, Mishra IK, Xie Y, Zhou H, Sun J, Zhou J, Ni Y, Luo D, Yu F, Yu Y, Chen S, Ren Z. Ternary Ni$_{2(1-x)}$Mo$_{2x}$P nanowire arrays toward efficient and stable hydrogen evolution electrocatalysis under large-current-density. Nano Energy. 2018;53:492. https://doi.org/10.1016/j.nanoen.2018.08.025.

[61] Yu C, Xu F, Luo L, Abbo HS, Titinchi SJJ, Shen PK, Tsiakaras P, Yin S. Bimetallic Ni-Co phosphide nanosheets self-supported on nickel foam as high-performance electrocatalyst for hydrogen evolution reaction. Electrochim Acta. 2019;317:191. https://doi.org/10.1016/j.electacta.2019.05.150.

[62] Menezes PW, Indra A, Zaharieva I, Walter C, Loos S, Hoffmann S, Schlögl R, Dau H, Driess M. Helical cobalt borophosphates to master durable overall water-splitting. Energy Environ Sci. 2019;12(3):988. https://doi.org/10.1039/C8EE01669K.

[63] Zhang C, Luo Y, Tan J, Yu Q, Yang F, Zhang Z, Yang L, Cheng H-M, Liu B. High-throughput production of cheap mineral-based two-dimensional electrocatalysts for high-current-density hydrogen evolution. Nat Commun. 2020;11(1):3724. https://doi.org/10.1038/s41467-020-17121-8.

[64] 8w?>Zhang L, Yan Z, Chen X, Yu M, Liu F, Cheng F, Chen J. Facile synthesis of amorphous MoS$_x$-Fe anchored on Zr-MOFs towards efficient and stable electrocatalytic hydrogen evolution. Chem Commun. 2020;56(18):2763. https://doi.org/10.1039/C9CC08771K.

[65] Liu R, Gong Z, Liu J, Dong J, Liao J, Liu H, Huang H, Liu J, Yan M, Huang K, Gong H, Zhu J, Cui C, Ye G, Fei H. Design of aligned porous carbon films with single-atom Co-N-C sites for high-current-density hydrogen generation. Adv Mater. 2021;33(41):2103533. https://doi.org/10.1002/adma.202103533.